ACS APPLIED MATERIALS & INTERFACES

www.acsami.org

Research Article

Designing Monoclinic Heterophase Coexistence for the Enhanced Piezoelectric Performance in Ternary Lead-Based Relaxor Ferroelectrics

Anyang Cui, Yan Ye, Kai Dai, Yawei Li, Liangqing Zhu, Kai Jiang, Liyan Shang, Guisheng Xu, Zhigao Hu,* Shujun Zhang, and Junhao Chu

Cite This: *ACS Appl. Mater. Interfaces* 2022, 14, 10535−10545

Read Online

ACCESS | Metrics & More | Article Recommendations | Supporting Information

ABSTRACT: Enhanced piezoelectric, dielectric properties and thermal stability in ternary relaxor-$PbTiO_3$ based ferroelectric crystals are expected to develop the next-generation of electromechanical devices. However, due to their increased disorder compared to other ferroelectrics, designing a controllable phase boundary structure and engineered domain remains a challenging task. Here, we construct a monoclinic heterophase coexisting in a ternary $Pb(In_{1/2}Nb_{1/2})O_3-Pb(Mg_{1/3}Nb_{2/3})O_3-PbTiO_3$ single crystal with optimized composition and an ultrahigh piezoelectric coefficient of 1400 pC N^{-1}, to quantify the correlation between spontaneous nanopolarity and phase heterogeneity, in an attempt to understand the origin of the exceptional functionalities. By designing an in situ high-resolution spectroscopic-microscopic technique, we have observed M_a and M_c heterophase mixtures spatially separated by the monoclinic heterophase boundary (MHB), which are responsible for the ferroelectric-dominated and relaxor-ferroelectric-dominated nanodomain structure, respectively. Internal energy mapping from optical soft mode dynamics reveals the inhomogeneous polarization and local symmetry on both sides of the MHB. Various molecular polarizabilities and localized octahedral distortions correlate directly with monoclinic regions and electromechanical contribution. This work clarifies the heterogeneity between structure, energy, and polar order and provides a new design freedom for advanced relaxor ferroelectrics.

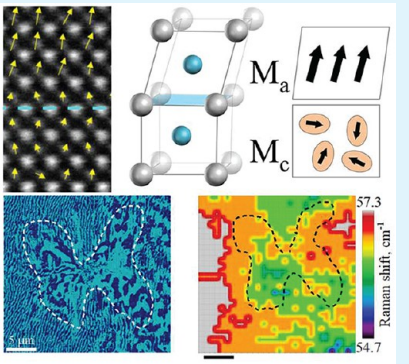

KEYWORDS: *relaxor ferroelectrics, nanostructure, nanodomain, phase coexistence, giant piezoelectricity*

INTRODUCTION

Relaxor ferroelectrics exhibit outstanding piezoelectric, dielectric, and optical properties and are suitable for the development of numerous electromechanical and photoacoustic applications.[1−5] Ternary $Pb(In_{1/2}Nb_{1/2})O_3-Pb(Mg_{1/3}Nb_{2/3})O_3-PbTiO_3$ (PIN-PMN-PT) shows a higher coercive field and better temperature stability than its binary $Pb(Mg_{1/3}Nb_{2/3})O_3-PbTiO_3$ (PMN-PT) counterpart.[3,6−8] However, designing the controllable structure and superior functionality of a ternary solid solution system has always been a challenge because of its increased chemical and polar disorders. To date, the morphotropic phase boundary (MPB) mechanism has been widely accepted for explaining the origin of the good performance in solid solution ferroelectric materials, while the existence of polar nanoregions (PNRs) in relaxor ferroelectrics breaks the long-range ferroelectric ordering with randomly oriented dipoles, greatly flattening the local free energy profile and contributing to the further enhanced properties.[9−13] Nevertheless, the underlying physical correlations between structure and polar orders remain to be explored.[14] Kalinin et al. reported the presence of both static and dynamic mesoscopic inhomogeneous regions in the ergodic relaxor phase by piezoresponse force microscopy (PFM), with the size being on the order of 100−200 nm.[9,15] Mesoscopic inhomogeneity is theoretically predicted in a simple thermodynamic way, showing the relationship between the diffuse phase transition and the local ferroelectric polarization distribution.[16] In addition, the structure mixture and complex polarization have been extensively studied from the micrometer scale to the nanometer scale.[4,17,18] This paradigm is expected to provide guidance for the structure design, domain engineering, and functionality improvement of relaxor PT-based materials.

Phase instability and transverse phonon localization are the main causes for the emergence of metastable monoclinic (M) phase bridging rhombohedral (R) and tetragonal (T) symmetries.[17,19−22] Intermediate M-symmetry (M_a, M_b, and

Received: November 26, 2021
Accepted: February 9, 2022
Published: February 17, 2022

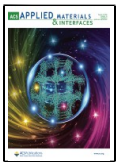

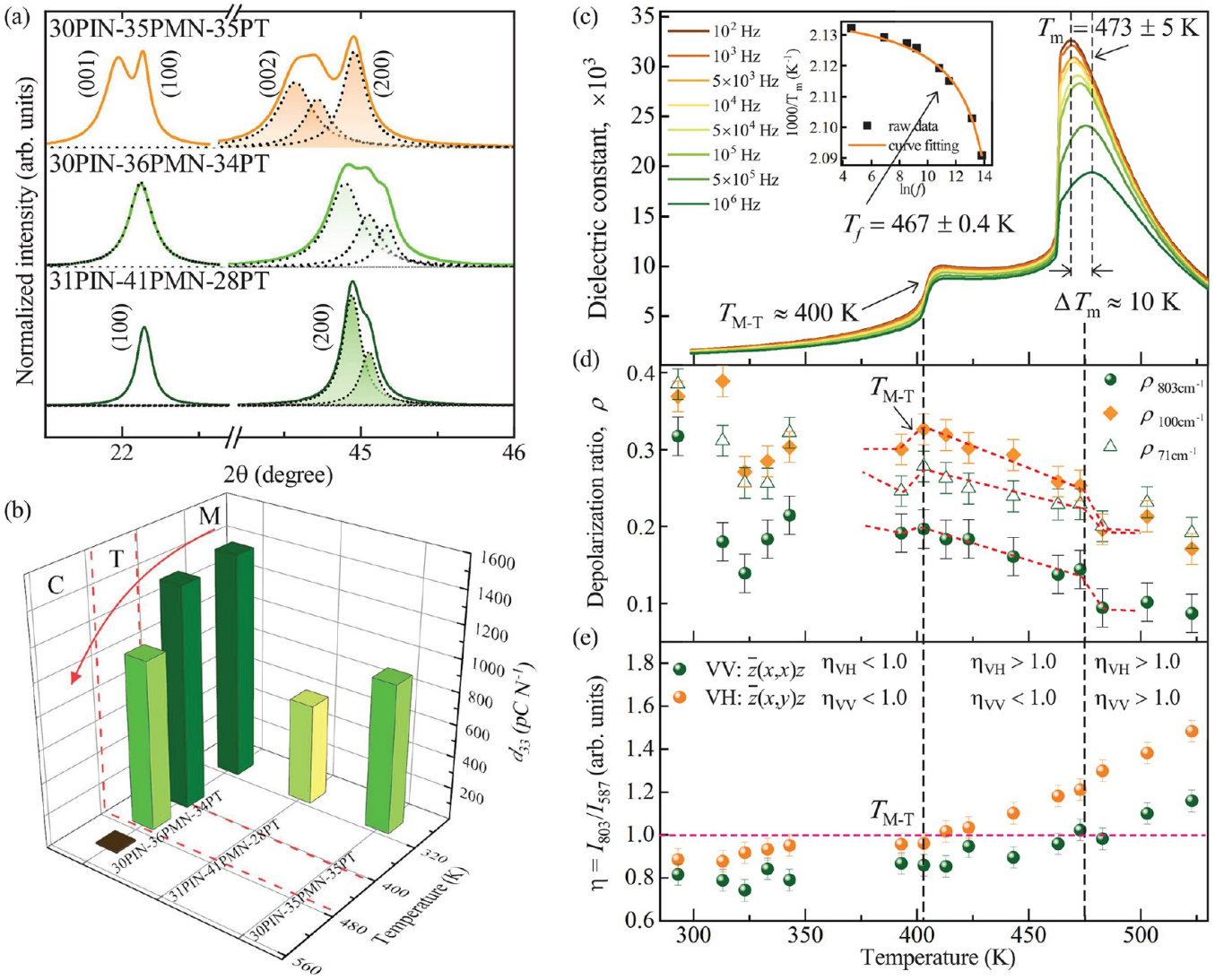

Figure 1. (a) XRD patterns with the diffraction peaks near $2\theta = 22°$ and 45° for 30PIN-35PMN-35PT, 30PIN-36PMN-34PT, and 31PIN-41PMN-28PT crystals, respectively. (b) d_{33} of three single crystals and its temperature dependence on monoclinic 30PIN-36PMN-34PT crystal. (c) High-temperature dielectric constant for 30PIN-36PMN-34PT single crystal. Inset plots the Vögel-Fulcher fitting. Temperature dependence of (d) depolarization ratio (ρ) and (e) Raman intensity ratio ($\eta = I_{803}/I_{587}$) in $\bar{z}(x,x)z$ and $\bar{z}(x,y)z$ polarized scattering geometries on the monoclinic 30PIN-36PMN-34PT crystal over temperature range of 290−530 K. All Raman spectra data obtained over the temperature range of 273−573 K are shown in Figure S1(b,c) of the SI.

M_c) groups are believed to balance the accommodated strain and favor the multidirectional polarization states at MPB.[20,23−26] The as-grown PMN-based relaxor ferroelectric crystal has a rhombohedral-like (R-like) M_a (space group *Cm*) and tetragonal-like (T-like) M_c (space group *Pm*) phases coexisting at room temperature, presenting an adjacent laminar domain structure.[22,27−31] It should be noted that exploring Pb-based ferroelectric performances requires consideration of the synergistic contributions from the lattice symmetry, polar order, and internal energy. Therefore, it is necessary to explore the spatial relationships between the structure, internal energy, and polarization disorder in Pb-based relaxor ferroelectrics with MPB composition, and to further strengthen the understanding of the structure-related piezoelectric contributions.

The natural interface between the T-like and R-like heterophase structure near MPB is related to the piezoelectric enhancement.[19,27] Here, we construct a monoclinic hetero-phase boundary (MHB) of M_a and M_c heterophases coexisting in a composition-modified PIN-PMN-PT single crystal, which shows the relaxor characteristics of frequency dispersion, diffuse phase transitions, and a stronger d_{33} of about 1400 pC N^{-1} over the crystals with pure phase. We systematically study the heterogeneous structure dynamics and in situ polar order behaviors. Complete pictures of the connection among polarization, heterophase, and the internal energy have been captured by in situ PFM coupled with the polarized micro-Raman imaging. It provides distinct evidence for explaining M_a/M_c phase variation, internal energy inhomogeneity, and the corresponding domain structure. Finally, the respective electromechanical contribution at each heterophase region is predicted. This work reveals that the monoclinic heterophase and the polarization inhomogeneity contribute to the increased the anisotropy degree, and provides a new strategy for designing advanced relaxor ferroelectrics.

https://doi.org/10.1021/acsami.1c22983
ACS Appl. Mater. Interfaces 2022, 14, 10535−10545

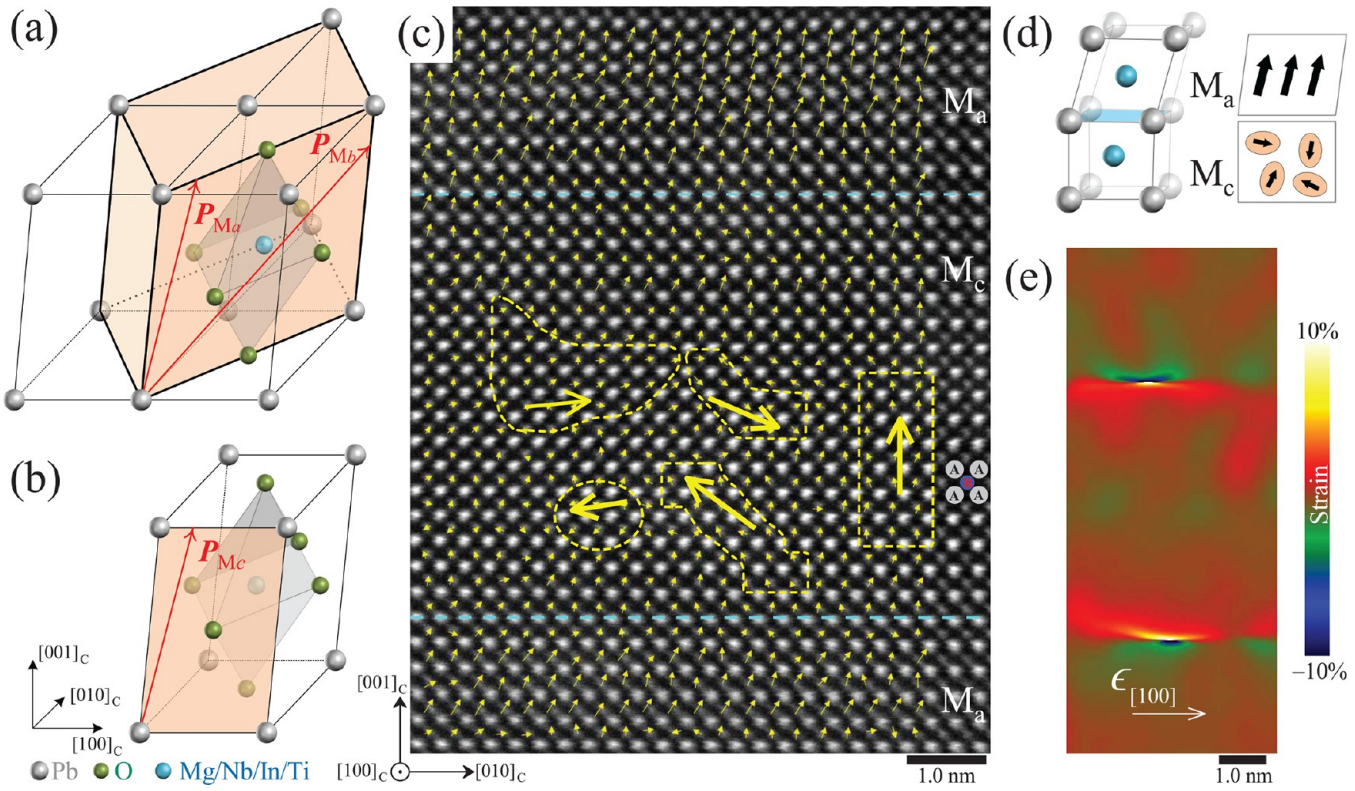

Figure 2. (a, b) Sketches of spontaneous polarizations (P_{M_a}, P_{M_b}, and P_{M_c}) in the monoclinic phase with respect to the pseudocubic unit cell. (c) HAADF-STEM image of the monoclinic PIN-PMN-PT single crystal. Yellow dashed lines indicate the nanodomains. The bright spots correspond to Pb columns, and the paler spots are the B-site cation columns. Yellow arrows indicate the displacement of B-site cation from the center of each cell. Blue dashed lines separate M_a and M_c heterophases. (d) Comparative display of the lattice configurations for M_a and M_c phases with their polarization states. (e) Strain map of a collected box area in (c). $\epsilon_{[100]}$ denotes the strain along the [100] direction.

RESULTS AND DISCUSSION

In order to obtain PIN-PMN-PT with monoclinic phase, as-grown $[001]_C$-oriented 30PIN-35PMN-35PT, 30PIN-36PMN-34PT, and 31PIN-41PMN-28PT single crystals were prepared by precisely controlling the stoichiometry. The basic structures were characterized by X-ray diffraction (Figure 1a) on single crystals, showing the sharp diffraction peaks. The 31PIN-41PMN-28PT crystal belongs to *R3m* space group of pure R phase, while the diffraction-peaks splitting into (100)/(001) and (200)/(002) confirm a pure T (*P4mm*) symmetry in 30PIN-35PMN-35PT. Between them, an intermediate phase noted as monoclinic (*m*) symmetry is found in 30PIN-36PMN-34PT with MPB composition[32,33,38] As shown in Figure 1b, pure R 31PIN-41PMN-28PT and pure T 30PIN-35PMN-35PT crystals have a piezoelectric coefficient of $d_{33} \approx$ 630 pC N^{-1} with about 920 pC N^{-1} at room temperature. Compared with the pure crystals, monoclinic 30PIN-36PMN-34PT generates a higher piezoelectric coefficient of about 1400 pC N^{-1} at room temperature and 400 K, and then decreases to 1050 pC N^{-1} at 450 K upon the increasing-temperature induced structural transition into T phase. With the temperature increases to 500 K, 30PIN-36PMN-34PT single crystal is paraelectric without the effective piezoelectric activity.

Figure 1c depicts temperature (T) dependent dielectric constant [$\varepsilon(f, T)$] on monoclinic PIN-PMN-PT. $\varepsilon(f, T)$ curve illustrates a diffuse phase transition from ergodic relaxor to ferroelectric phase near 470 K, and ferroelectric-ferroelectric phase transition near 410 K noted as T_{M-T}. To quantify the frequency dispersion behavior, the maximum temperature of ε_{max} (T_m) around 473 K with $\Delta T_m \approx 10$ K over frequency range of 10^2 to 10^6 Hz is fitted by the Vögel-Fulcher law $f = f_0 e^{-U_a/k_B(T_m - T_f)}$,[34,35] where the activation energy U_a of 33.5 meV and the static freezing temperature T_f of about 467 K are achieved. It implies that the monoclinic PIN-PMN-PT holds the enhanced relaxation and predicts a strong PNR interaction.[36,37]

To explore the heterophase structure, internal energy, and temperature stability, we employ the unpolarized and polarized Raman spectroscopy in the cross-polarized VH: $\bar{z}(x,y)z$ and parallel-polarized VV: $\bar{z}(x,x)z$ geometries. Room temperature Raman spectra were shown in Figure S1(a) (see the Supporting Information, SI). Raman-active vibrations extracted by fitting process show 12 modes on cubic (C) PIN-PMN-PT, involving the transverse optic (TO) and longitudinal optic (LO) of $3T_{1u}+T_{2u}$ modes. The observed modes have been assigned and marked in $\bar{z}(x,y)z$ spectra, well matching with the reported experimental and calculated phonon recognition.[38−40] Owing to the anisotropy and nonsymmetric second-order polarizability of PIN-PMN-PT lattice, obvious spectral variations among the unpolarized, $\bar{z}(x,x)z$, and $\bar{z}(x,y)z$ scattering can be seen, especially for the Pb-BO_6 stretching modes at low wavenumber range of 30−150 cm^{-1}. A breathing mode near 55 cm^{-1} is very strong in $\bar{z}(x,y)z$ geometry, but is silent in $\bar{z}(x,x)z$. In addition, the modes at 150−500 cm^{-1} are derived from the mixed B−O−B bending and O−B−O stretching behaviors in BO_6 octahedra, while the B−O−B bending also contributes to the vibrational signals at 500−900 cm^{-1}.

https://doi.org/10.1021/acsami.1c22983
ACS Appl. Mater. Interfaces 2022, 14, 10535−10545

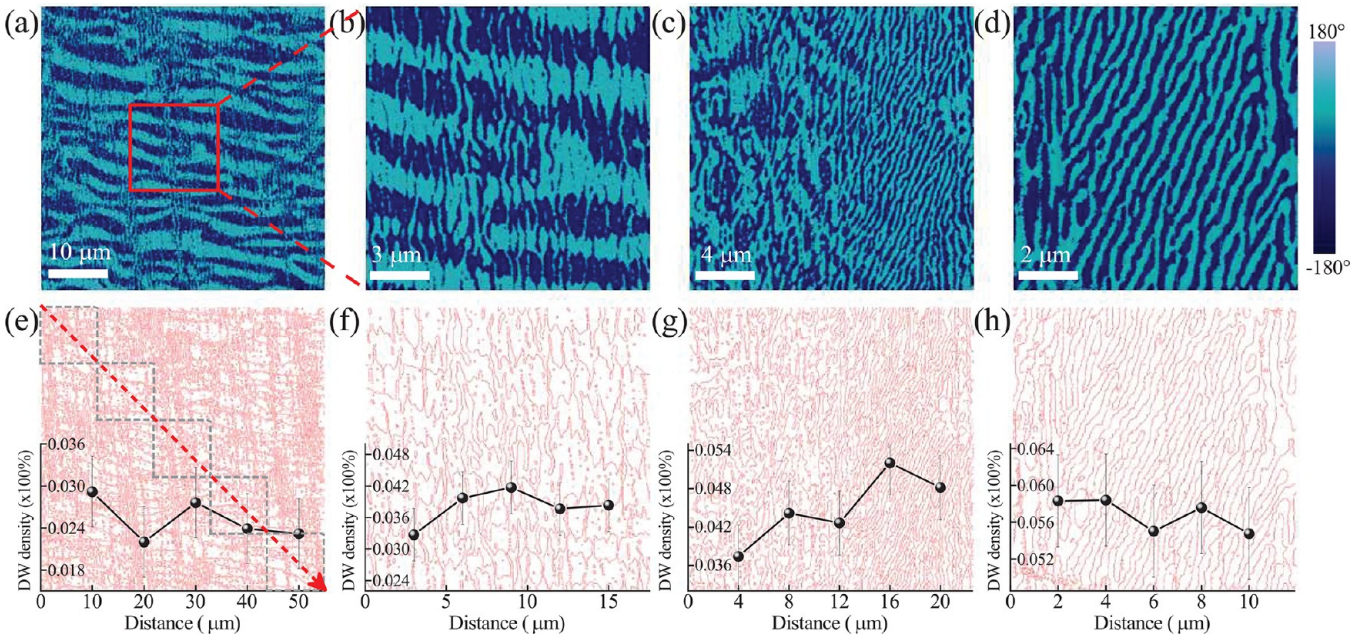

Figure 3. (a–d) Out-of-plane phase images of PFM on the different random-chosen 3 areas of crystalline (001) face of 30PIN-36PMN-34PT single crystal at MPB. (e–h) Ferroelectric domain wall (DW) distribution images obtained on the corresponding phase signal (a–d) by the gradient-filter method, respectively. The insets are the respective DW density profile curves collected from five sequential square areas along the diagonal of image as marked by the dashed red arrow in (e).

Our previous reports[41−43] have revealed that the depolarization ratio can reflect the molecular symmetry difference and lattice variation of ferroelectric perovskites, following the formula of the polarized Raman scattering intensity ratio $\rho = \frac{I_{\bar{z}(x,y)z}}{I_{\bar{z}(x,x)z}}$. The temperature dependent depolarization ρ value of the vibrational modes around 71, 100, and 803 cm^{-1} in Figure 1d fluctuates first at 293−343 K corresponding to the instable monoclinic phase. The depolarization fluctuation near room temperature illustrates the unstable lattice polarizability,[30] which would be attributed to the monoclinic symmetry with unstable phase coexistence. An abrupt increase near 400 K confirms the phase transition (T_{M-T}) from monoclinic to T phase. Similarly, the change of ρ value near 473 K indicates the critical temperature of T_m. Moreover, diffuse phase transformation of monoclinic PIN-PMN-PT could be distinguished by calculating the intensity ratio $\eta = I_{803}/I_{587}$ in VV and VH configurations:[29] $\eta_{VH} < 1$ and $\eta_{VV} < 1$ in monoclinic phase, $\eta_{VH} > 1$ and $\eta_{VV} < 1$ in T phase, and $\eta_{VH} > 1$ and $\eta_{VV} > 1$ in C phase, respectively, where the peak around 587 cm^{-1} is associated with A_1(TO) mode in T phase and A′′ mode in monoclinic phase. As shown in Figure 1e, the temperature dependence of $\eta = I_{803}/I_{587}$ represents M → T → C phase transition process. Therefore, by studying the soft-mode thermodynamics and depolarization fluctuation, the room temperature monoclinic phase of PIN-PMN-PT as an adaptive structure exhibits structural instability.

In this metastable intermediate structure bridging R and T symmetries, the monoclinic polarization orientation is constrained to a crystallographic plane, rather than a crystallographic axis. The M_a lattice is rotated by 45° about the $[001]_C$ direction with respect to the pseudocubic cell, where P_{M_a} lies along the $[uuv]$ direction ($u > v$) in the $(1\bar{1}0)_C$ plane (Figure 2a), whereas M_c allows the spontaneous polarization P_{M_c} along the $[u0v]$ direction ($u \neq v$) in the $(010)_C$ plane (Figure 2b). Strong polarization would contribute to the variation of octahedral distortion and lattice anisotropy in M_a and M_c phases. The heterophase region was examined at atomic resolution using high-angle annular dark field scanning transmission electron microscopy (HAADF-STEM) in Figure 2c. The polarization, lattice distortion, and in-plane strain variations of the HAADF-STEM-measured area have been studied to reveal the nanoscale coexistence of M_a and M_c heterophases. Local polarization within the ABO_3 lattice can be obtained by calculating the projected displacement of B-site cations relative to the center of four neighboring Pb cations.[4,19,44,45] Octahedral distortion behavior shows an obvious tilting in M_a, whose polarization configurations behave more orderly. For M_c regions, the polar order is more complex. Its domain size decreases to several nanometers, behaving more disorderly. We roughly delineated nanopolar regions with yellow dashed lines. Hence, there are clear interfaces separating the M_a and M_c regions with the different polarization states, in terms of the polar magnitude and polar orientation.

We define the interface as monoclinic heterophase boundary (MHB), which is marked by blue dashed lines in Figure 2c. As sketched in Figure 2d, the M_a lattice generally tilts along the $[010]_C$ axis and presents a generally ordered polarization orientation, while the M_c region exhibits the local polar heterogeneity distribution. Because a small magnitude of atomic displacement in the measured $(010)_C$ plane may exhibit large polarization along the other crystalline axes, the arrow length cannot in reality reflect the polarization magnitude for the adjacent M_a and M_c heterophases. Furthermore, the heterophase structure is also clearly observed in the geometric phase analysis (GPA) strain image along $[001]_C$ (Figure 2e) of the chosen box region, where GPA is an effective method to reflect the structural variation in an area of the STEM image. Around the M_a and M_c heterophase boundary, the lattice is incoherently strained in the in-plane direction. The sharp

https://doi.org/10.1021/acsami.1c22983
ACS Appl. Mater. Interfaces 2022, 14, 10535−10545

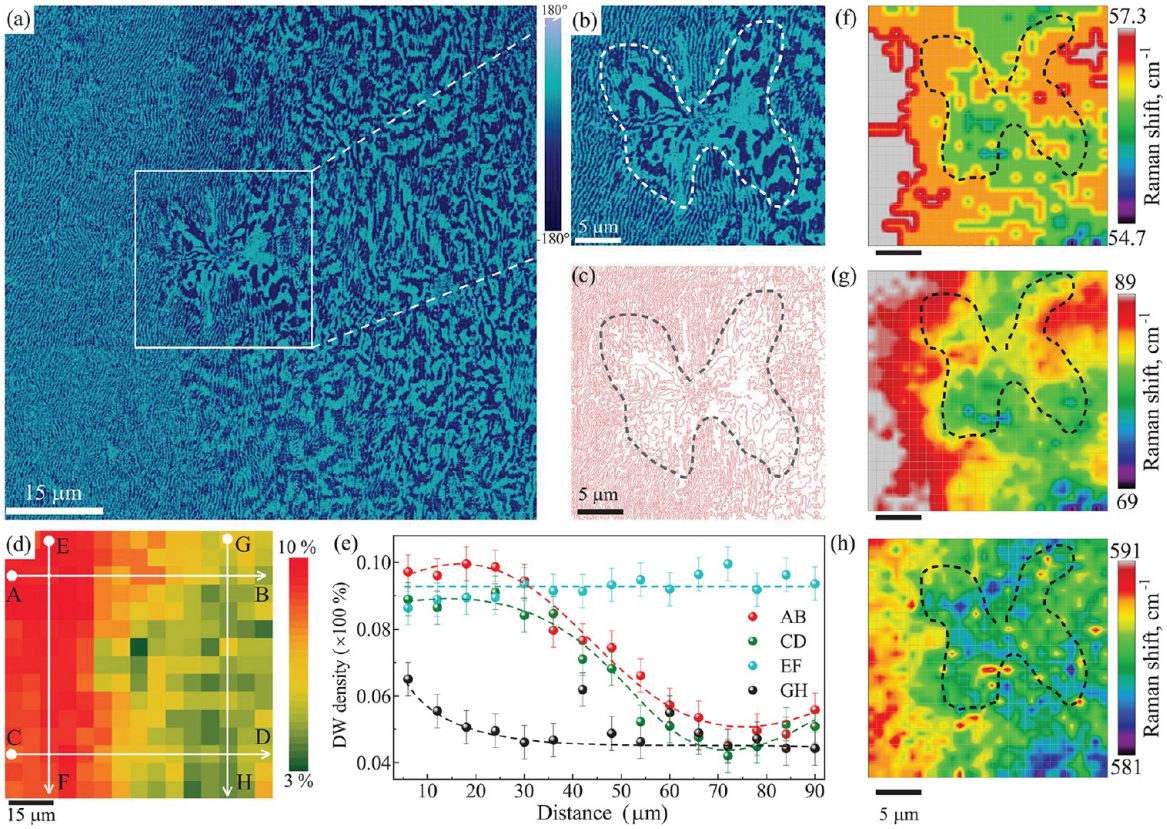

Figure 4. Out-of-plane PFM phase image (a) with the size of 90 μm and (b) with the enlarged box with the size of 30 μm. (c) Domain wall (DW) distribution of image (b) obtained by gradient-filter method. (d) A calculated DW density distribution (90 μm). Each density pixel counts the proportion of DW points in each equally distributed 5 μm area of image (a). (e) Four corresponding line profiles of DW density along the arrows in (d). (f–h) Raman frequency images around 55, 80, and 585 cm^{-1}, respectively, from micro-Raman spectral mapping in $\bar{z}(x,y)z$ polarized scattering geometry. The dashed lines sketch the separation boundary of different domain morphologies.

mutation of the in-plane strain variation occurs at the heterophase boundary MHB, due to the changing lattice constants between M_a and M_c symmetry. Therefore, STEM results provide direct evidence about the monoclinic heterophase coexistence and complex polar disorder on the atomic-resolved scale.

On the micrometer scale, ferroelectric domains in M_a and M_c regions and their spatial distribution dependence were investigated by PFM. Domain variation in monoclinic phase is associated with the rotational polarization instability, contributing to the crystallographic anisotropy variation of the polarization orientation.[14,46,47] PFM results (see Figure S2 in the SI) indicate the ribbon-shaped out-of-plane domain textures on the [001]-oriented crystals with pure R and T phases. Figure 3 illustrates the out-of-plane ferroelectric domains on the randomly chosen regions in the monoclinic 30PIN-36PMN-34PT crystal. Both the ribbon-shaped domain structure and the irregular texture can spontaneously distribute spatially in two forms: the nanodomain-in-microdomain configuration (see Figure 3a,b) and the coexistence distribution separated by clear boundaries (Figure 3c), showing that the nanoscale domain ripples intersect vertically with the micrometer-scale ribbon-shaped domains. The variation of domain configuration implies that MHB on the micrometer scale possibly belongs to a polarization-misfit interface. Domain formation in this case is associated with the accommodation of the misfit-generated stress and internal electric field of the PIN-PMN-PT crystal, resulting in the reduction of domain wall (DW) energy. Hence, the DW distribution is extracted from the phase channel pixel by pixel using a gradient-filter model, so that the normalized DW density can be statistically estimated by counting percentage of pixel at DW location. Figure 3e–h illustrates the corresponding DW distributions and their DW density profiles in each inset, which are achieved by calculating the average DW density in five sequential square areas along the diagonal of each image. Figure 3g can clearly show the comparison of DW density between the ribbon-shaped domain area and the irregular domain, in which the former has a larger density of about 5.0% than the latter of 4.0%. These domain scenarios in the monoclinic crystal reflect the inhomogeneous polar order of PIN-PMN-PT, due to the heterophase coexistence.

Figure 4a,b shows out-of-plane domains in a 90 μm area and its 30 μm enlarged zone, respectively, clearly illustrating the regular ribbon-shaped domain morphology on the left and the irregular one on the right. Differing from pure phase crystals, domains of the monoclinic phase present the distinct spatial distribution dependence. Figure 4c,d shows DW distribution (30 μm) and the quantified DW density image (90 μm), corresponding to Figure 4b,a, respectively. Combined with the density profiles (Figure 4e) extracted along the marked arrows in Figure 4d, the ribbon-shaped domain presents a high wall density of about 9.0%, while the irregular domain presents the island-shaped disordered DW configuration with a reduced density of about 5.0%. Being analogous to the classic ferroelastic microstructure of polydomain plates,[48] the

https://doi.org/10.1021/acsami.1c22983
ACS Appl. Mater. Interfaces 2022, 14, 10535−10545

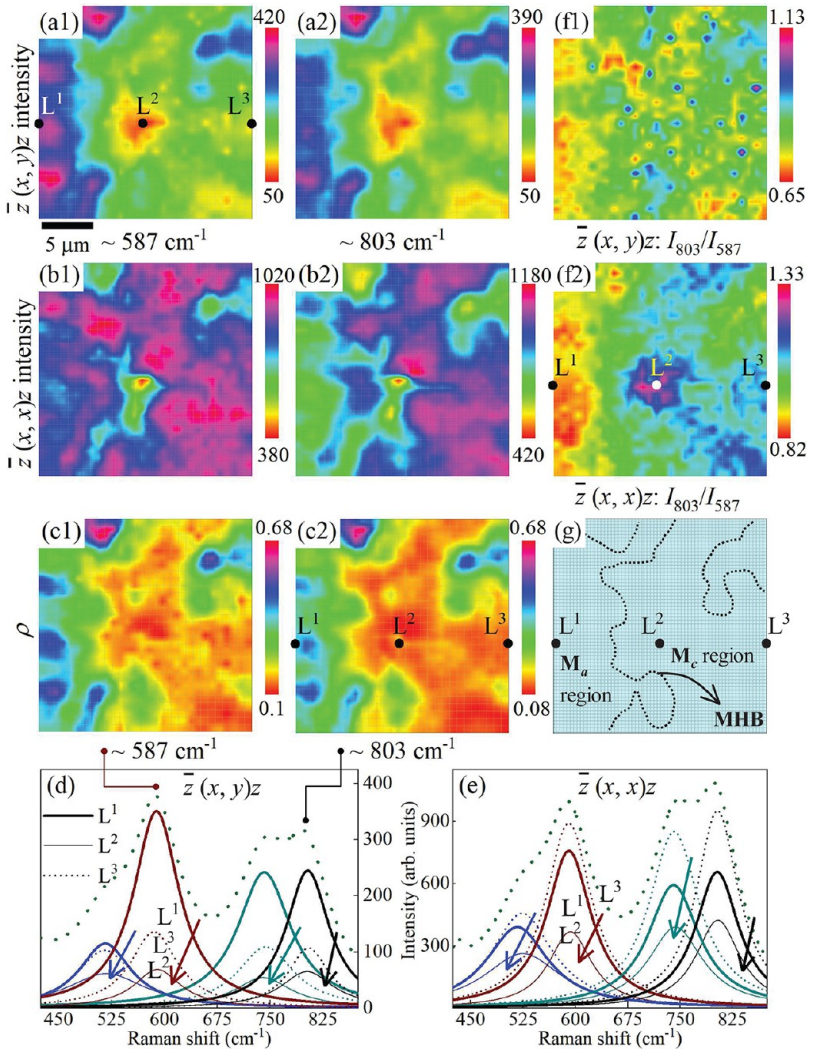

Figure 5. In situ Raman scattering intensity maps of the representative modes around 587 and 803 cm^{-1} in the polarized (a) VH: $\bar{z}(x,y)z$ and (b) VV: $\bar{z}(x,x)z$ geometries. (c) Maps of depolarization ratio (ρ) for the corresponding vibration modes. (d, e) The fitted scattering peaks in both polarized geometries at the marked spots [L^1 (solid thick line), L^2 (solid thin line), and L^3 (dotted thin line)]. (f) Maps of intensity ratio ($\eta = I_{803}/I_{587}$). (g) A schematic of the proposed phase distribution in the measured 30 μm area.

structure difference affects the size of domain distribution to control the misfit-generated long-range stress in the inhomogeneous lattice.[27,46] The observed domain heterogeneity for stress accommodation will meet the energy minimization requirement of the system, including lattice strain (elastic), interfacial energy (gradient), and electrostatic energy minimization. Under this circumstance, the DW energy density γ is related to the domain size λ_0 and the thickness (t) of the domain layer, following $\gamma = \frac{\lambda_0^2 \mu \epsilon_0^2}{pt}$, where p is a constant, and μ and ϵ_0 are the shear modulus and twinning strain, respectively.[46,49] So the decreased wall density ($\propto 1/\lambda_0$) of the ferroelectric domain reflects the growing DW energy density γ. In monoclinic PIN-PMN-PT, the ribbon-shaped domain region in Figure 4a possesses a lower DW energy density γ than the irregular domain area. Therefore, the different microdomain laminas are of the varied DW density and DW energy in the PIN-PMN-PT crystal with MPB composition.

On the basis of the observations of TEM and PFM, the ferroelectric domain variation is closely related to its mixed M_a and M_c phase coexistence on the nano-to-micro scale. Heterophases in relaxor ferroelectrics lead to the misfit stress of lattice and consequently allow polarization heterogeneity for accommodating the stress.[29,31] The connections between polarizataion and structure were studied on the same region of Figure 4b by in situ micro-Raman imaging. Raman spectroscopy has a high sensitivity to the spatial phase variation by analyzing the soft-mode.[28,29,50] Under the same ambient pressure and temperature, the phonon frequency shift is mainly attributed to the intrinsic phase difference and the internal stress inhomogeneity.[51,52] Phonon frequency mappings around 55, 80, and 585 cm^{-1} in Figure 4f–h, respectively, clearly show a larger frequency on the left side, associating with the ribbon-shaped domain configuration, while the irregular domain area corresponds to the smaller frequency values. Similarly, Hlinka et al.[27] reported a macroscopic lamellar structure in PMN-0.32PT by polarized Raman spectroscopy, indicating an array of "morphotropic" interphase boundaries between R-like and T-like areas. Therefore, Raman images initially reveal that the observed lamellar domain heterogeneity is consistent with different phase structures or the effect of the nonuniform internal stress in monoclinic PIN-PMN-PT. However, it should be noted that

https://doi.org/10.1021/acsami.1c22983
ACS Appl. Mater. Interfaces 2022, 14, 10535−10545

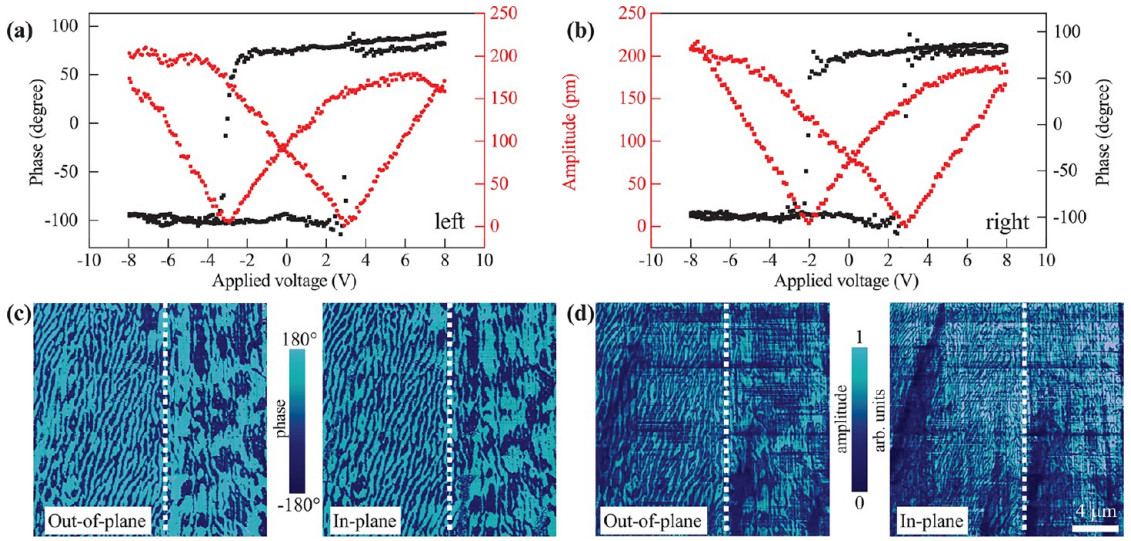

Figure 6. (a, b) Amplitude-voltage butterfly and phase-voltage hysteresis loops obtained by PFM switching measurements on the left and right zones of (c) phase and (d) amplitude images on the unpoled monoclinic PIN-PMN-PT single crystal. The white dashed lines mark the MHB location and separate the regions with left labyrinthine and right irregular domain patterns. Domain images include out-of-plane and in-plane domain images. Scan size is 20 μm.

phonon frequency in theory cannot be directly used for M_a and M_c heterophase recognition.

To explore the spatial distribution of lattice symmetry and anisotropy, the polarized Raman images were further obtained in this heterophase region. The polarized scattering intensity is proportional to the molecular polarizability α_{ij} (C m^2 V^{-1}), following $I_{\overline{z}(i,j)z} \propto \frac{16\pi^4 v^4}{c^4}\alpha_{ji}^2 I_0$, where c is light velocity in vacuum, and I_0 is the incident energy.[43] Figure 5a,b presents the $\overline{z}(x,y)z$ and $\overline{z}(x,x)z$ scattering intensity images of the main phonon around 587 and 803 cm^{-1}. To highlight the difference of scattering characteristics among the different positions, three representative areas are chosen and marked as L^1, L^2, and L^3 sites. Figure 5d,e plots the position dependence of the fitted Raman spectra. $\overline{z}(x,y)z$ scattering intensity is larger around L^1 than that around L^2–L^3 ($I_{L^1}^{VH} > I_{L^3}^{VH}$), while the region around L^3 becomes stronger scattering in the $\overline{z}(x,x)z$ geometry ($I_{L^3}^{VV} > I_{L^1}^{VV}$). Intensities from both cross and parallel-polarized scattering appear the weakest value at the region (L^2) around the center, which is coincidentally located at the domain center surrounded by long-range ribbon-shaped domains and irregular ones shown in Figure 4b. Simultaneously, Figure S3 in the SI shows the consistent frequency shift behavior of the polarized Raman bands around 587 and 803 cm^{-1}. Inhomogeneous intensity mapping results from the polarizability variation of lattice and consequently presents a rough outline of the distinguished anisotropy distribution with a spatial resolution of about 1 μm.

Theoretically, the crossed $\overline{z}(x,y)z$ scattering originates from the x-to-y distortion in the electric-field direction of the incident light due to the anisotropic perovskite polarizability. The calculated depolarization ratio ρ value represents the lattice symmetry and the anisotropy degree distribution of PIN-PMN-PT crystal, where the value approaching 0.75 (the maximum value) reflects the enhanced anisotropy.[43] As illustrated in Figure 5c, it shows a lower ρ value around L^2 and L^3 sites comparing to that at L^1. Combining the scattering intensity images, we find that the area around L^1 shows the larger anisotropy and octahedral distortion degree than L^2 and L^3 regions. The MHB separates regions with various anisotropy and symmetry. Moreover, peak competition quantified by the scattering intensity ratio can be used to recognize the coexistent M_a and M_c heterophases, and also minimize effects from instrumental conditions.[29] Intensity ratio ($\eta = I_{803}/I_{587}$) maps in $\overline{z}(x,y)z$ (Figure 5f1) and $\overline{z}(x,x)z$ (Figure 5f2) configurations further confirm the spatial inhomogeneity, showing $\eta < 1$ at L^1 and $\eta_{VV} > 1$ at L^2.

The M_a and M_c coexistence separated by MHB has been revealed by the consistent images of phonon frequency, molecular polarizability, and lattice symmetry. Heterophase and MHB structure confirm the theoretical prediction of eighth-order Devonshire-Landau free energy expansion, which clarifies the structure variation of low-symmetric M_a and the more spherical-symmetric M_c subphases in the unit sphere space.[24] The intrinsic monoclinic polarization leads to a stronger lattice distortion and polarizability difference in M_a than in M_c. Hence, it directly explains that the L^1 region will follow M_a symmetry, while the L^2-L^3 areas belong to M_c. In other words, a high depolarization value and a low intensity ratio illustrate a low-symmetric M_a phase, while the neighboring L^3 region turns into the more symmetric M_c phase instead. Figure 5g sketches the M_a and M_c heterophase distribution on micrometer scale, separated by the MHB, which simultaneously separate various microdomain configurations with different DW energy. Ribbon-shaped domain in low-symmetric M_a region holds higher DW density and lower DW energy, when comparing to the irregular domain texture on high-symmetric M_c. The observed multidomain textures have been successfully modeled in the structural heterophase laminates, allowing the minimization of the internal energy of the crystal, including the elastic, electrical, and the domain interface energies.[53,54] Therefore, the qualitative DW energy in the distinct domain regions, as one of the key components of the total internal energy, may interpret the heterophase dependent energy distribution at the MHB region.

The coexistent heterophases and the architecture of MHB on the nano-to-micro scale in relaxor materials with composition close to MPB is regarded as the significant factor

https://doi.org/10.1021/acsami.1c22983
ACS Appl. Mater. Interfaces 2022, 14, 10535−10545

in the piezoelectric enhancement. Macroscopic two-phase laminates and nanoscale heterophase structures have been observed on Pb-based relaxor ferroelectrics and $BiFeO_3$ films for the strain accommodation by forming distinct polar variants.[19,22,27] Local piezoelectric response is estimated by amplitude-voltage butterfly loops and amplitude images by the vertical PFM method, as shown in Figure 6. The measured piezoresponse does not show the obvious difference in amplitude on the left (M_a) and right (M_c) sides of MHB. Generally, the piezoelectric response of Pb-based relaxor ferroelectrics can be improved by electric poling along the $[001]_C$ crystallographic direction in R or O phase. Through estimating the degree of short-range order from Raman spectra,[18] it is explained that the ribbon-shaped domain on the $[011]_C$-poled relaxor-PT based crystal exhibits weaker piezoresponse than the $[001]_C$-poled one. However, comparing the intrinsic piezoelectric contributions of the M_a or M_c phase for the unpoled PIN-PMN-PT should consider lattice structure and internal energy properties, rather than the domain switching effect.[55] According to the Landau phenomenological theory,[14,44,56] the polarization anisotropy and energy barrier between the various polarization states in the nanodomain of an intermediate phase will be greatly weakened, leading to a flatter Landau energy profile than that of the pure R or T structure. Combining the Raman scattering results for microscopic structure analysis and TEM results of nanoscale polar features, it is observed that compared with the M_a region, the M_c phase exhibits reduced nanodomain size, higher domain wall energy, and lower free energy for polarization rotation. Therefore, for ternary PIN-PMN-PT, the contribution of the M_c phase to the piezoelectric property is greater than that of the M_a phase.

CONCLUSIONS

In conclusion, a ternary PIN-PMN-PT relaxor ferroelectric crystal with a monoclinic phase was studied, where an MHB spatially separates the adaptive M_a and M_c heterophases, in which the variation of the laminar ferroelectric domain structures are associated with the different domain wall energy, polarization rotation free energy, molecular polarizability, and symmetry. The interface at MHB will generate the misfit stress and asymmetric electric field. The nano-to-microscale M_a and M_c heterophases allow the intrinsic polarization rotation free energy instability with the polymorphic nanodomain states. The ribbon-shaped domain with larger DW density is observed at the low-symmetric M_a phase region, while the irregular domain texture with the decreased DW density exists at the higher spherical-symmetric M_c phase region. The heterogeneous phase coexistence and polar orders with distinct direction variants meet the requirement of strain accommodation. Internal strain accommodation leads to different domain configurations and domain wall energies of M_a and M_c areas. According to the relationship between the local heterogeneous M_a and M_c symmetries and their nanopolar domains, we reveal that the M_c polymorphic nanodomain structure contributes more to the enhanced electromechanical property. This work provides a new idea for understanding the origin of the large piezoelectric response, guiding the structure design and piezoelectric enhancement of relaxor ferroelectric material systems.

EXPERIMENTAL SECTION

Preparation of PIN-PMN-PT Single Crystal Samples. Ternary $Pb(In_{1/2}Nb_{1/2})O_3-Pb(Mg_{1/3}Nb_{2/3})O_3-PbTiO_3$ (PIN-PMN-PT) single crystals were grown using the modified Bridgman method, with details reported by Xu et al.[57] As-grown single crystals were oriented to the crystallographic [001] direction and cut into plate samples with sizes of 10 × 10 × 0.45 mm^3. The unpoled sample surface was mechanically polished.

HAADF-STEM. STEM specimen was prepared with a dual-beam focused ion beam (FIB) system (Nanolab Helios 650) using Ga ion accelerating voltage (30 kV). Then, ion-milling operation was implemented from 24 pA to 9.3 nA. The HAADF-STEM images were captured using the STEM mode of a JEM Grand ARM300F microscope with double spherical aberration (Cs) correctors operated at 300 kV. A probe convergence angle of 24 mrad and the detection angles of 63−180 mrad were applied.

XRD, Dielectric, and Piezoelectric Constant Characterization. X-ray diffractometer (XRD, Cu Kα, D8 Advance, Bruker) was employed to reveal the crystal structures. Temperature dependence of dielectric constant at a temperature range from room temperature to 570 K were carried out at 10^2 to 10^6 Hz using an impedance analyzer (Keysight Technologies E4990A). Piezoelectric constant (d_{33}) was measured after poling under 2 kV/mm DC fields at 170 °C for 15 min in silicon oil using a quasi-static piezo-d33 m (ZJ-6A, Institute of Acoustics, Chinese Academy of Sciences, Beijing, China).

PFM. To observe the spontaneous domain texture and the switching dynamics, PFM tests in contact mode and DataCube-PFM mode[58] were implemented on a commercial scanning probe microscopy system (Dimension Icon, Bruker) equipped with a controller including a function generator and lock-in amplifier. A conductive diamond coated probe (DDESP-V2) with a spring constant of ~80 N/m and a resonant frequency of about 450 kHz (Nom.) was used in contact mode. The observed PFM response was collected by applying an AC drive-voltage at the low frequency of 25−30 kHz and the amplitude of 2.5−5 V on sample, which was attached on a polished metal disc by conductive silver paint as the bottom electrode. PFM phase and amplitude images were obtained with a pixel of 256 × 256. An image process method of gradient-filter algorithm has been employed to extract the domain wall distribution by calculating the discrete derivative ($d\phi/dx$ and $d\phi/dy$) of the PFM phase signal (ϕ) to an approximate gradient $g(\phi)$ at pixels reflecting the phase mutation region. According to the achieved domain wall distribution image, the domain wall density can be figured out by counting the percentage of the pixel at the domain wall location in a unit range.

Raman Spectroscopy and Micro-Raman Scattering Mapping. The unpolarized and polarized Raman spectra and mapping data were carried out on a Jobin-Yvon LabRAM HR Evolution micro-Raman spectrometer with a Linkam THMSE 600 heating/cooling stage with a rate of 10 K/min and an accuracy of ±0.1 K. The spectral resolution was better than 1 cm^{-1}. The wavelength of the excitation source was 532 nm. Laser-induced heating effect can be eliminated due to the weak energy of about 4 mW on the measured surface. An objective lens of 100× and NA = 0.90 was employed to focus the 532 nm light beam to the spot size of approximately 0.72 μm. In situ micro-Raman mapping realizes the same repeatedly measured site by mounting the sample on a motorized *xy*-stage with a move step-size of 1 μm. Hence, the spatial resolution of Raman imaging is estimated at about 1 μm. A Piezo XY-Nanopositioning Stage [Physik Instrumente (PI)] was employed to realize in situ imaging measurements of scanning probe microscopy and Raman spectroscopy.

The polarized scattering spectra and mappings use the polarizers placed in the excitation and detection path to define the paralleled-polarized (VV) and the crossed-polarized (VH) scattering geometries. The polarized Raman scattering can control the propagation (k_i, k_s) and electrical-field (E_i, E_s) directions of the incident and scattered light. The classic notation for describing the polarized scattering geometry is Porto's notation,[59] $k_i(E_i, E_s)k_s$, which is used to express the orientation of the crystal with respect to the polarization of the

https://doi.org/10.1021/acsami.1c22983
ACS Appl. Mater. Interfaces 2022, 14, 10535−10545

laser in both the exciting and analyzing directions.[43] The backscattering Raman spectroscopy used in our work needs the direction relations of $k_i = -k_s$, $k_i \perp E_i$, and $k_s \perp E_s$. Raman spectra in the VV and VH geometries were recorded on the polished (001)-cut PIN-PMN-PT crystals. We assume that the axes x, y, and z are parallel to the cubic [100], [010], and [001] directions. The scattering light is collected by an analyzer, which is oriented either VV or VH to the polarization of the incident laser, thus corresponding to $\bar{z}(x,x)z$ and $\bar{z}(x,y)z$ geometries, respectively.

■ ASSOCIATED CONTENT

Supporting Information

The Supporting Information is available free of charge at https://pubs.acs.org/doi/10.1021/acsami.1c22983.

Figures S1−S3, room temperature Raman spectra with their fitting results, temperature dependent Raman spectra at 273−573 K, PFM phase images on three PIN-PMN-PT single crystals, and the frequency images of the polarized-Raman bands around 587 and 803 cm^{-1} (PDF)

■ AUTHOR INFORMATION

Corresponding Author

Zhigao Hu − *Technical Center for Multifunctional Magneto-Optical Spectroscopy (Shanghai), Engineering Research Center of Nanophotonics & Advanced Instrument (Ministry of Education), Department of Materials, School of Physics and Electronic Science, East China Normal University, Shanghai 200241, P. R. China; Collaborative Innovation Center of Extreme Optics, Shanxi University, Taiyuan, Shanxi 030006, P. R. China; Shanghai Institute of Intelligent Electronics & Systems, Fudan University, Shanghai 200433, P. R. China;* orcid.org/0000-0003-0575-2191; Email: zghu@ee.ecnu.edu.cn

Authors

Anyang Cui − *Technical Center for Multifunctional Magneto-Optical Spectroscopy (Shanghai), Engineering Research Center of Nanophotonics & Advanced Instrument (Ministry of Education), Department of Materials, School of Physics and Electronic Science, East China Normal University, Shanghai 200241, P. R. China*

Yan Ye − *Technical Center for Multifunctional Magneto-Optical Spectroscopy (Shanghai), Engineering Research Center of Nanophotonics & Advanced Instrument (Ministry of Education), Department of Materials, School of Physics and Electronic Science, East China Normal University, Shanghai 200241, P. R. China*

Kai Dai − *Technical Center for Multifunctional Magneto-Optical Spectroscopy (Shanghai), Engineering Research Center of Nanophotonics & Advanced Instrument (Ministry of Education), Department of Materials, School of Physics and Electronic Science, East China Normal University, Shanghai 200241, P. R. China*

Yawei Li − *Technical Center for Multifunctional Magneto-Optical Spectroscopy (Shanghai), Engineering Research Center of Nanophotonics & Advanced Instrument (Ministry of Education), Department of Materials, School of Physics and Electronic Science, East China Normal University, Shanghai 200241, P. R. China;* orcid.org/0000-0001-8776-5687

Liangqing Zhu − *Technical Center for Multifunctional Magneto-Optical Spectroscopy (Shanghai), Engineering Research Center of Nanophotonics & Advanced Instrument (Ministry of Education), Department of Materials, School of Physics and Electronic Science, East China Normal University, Shanghai 200241, P. R. China*

Kai Jiang − *Technical Center for Multifunctional Magneto-Optical Spectroscopy (Shanghai), Engineering Research Center of Nanophotonics & Advanced Instrument (Ministry of Education), Department of Materials, School of Physics and Electronic Science, East China Normal University, Shanghai 200241, P. R. China*

Liyan Shang − *Technical Center for Multifunctional Magneto-Optical Spectroscopy (Shanghai), Engineering Research Center of Nanophotonics & Advanced Instrument (Ministry of Education), Department of Materials, School of Physics and Electronic Science, East China Normal University, Shanghai 200241, P. R. China;* orcid.org/0000-0003-2341-3978

Guisheng Xu − *R&D Center of Synthetic Crystals, Chinese Academy of Sciences Shanghai Institute of Ceramics, Shanghai 201899, P. R. China*

Shujun Zhang − *Institute for Superconducting and Electronic Materials, Australian Institute for Innovative Materials, University of Wollongong, Wollongong, New South Wales 2500, Australia;* orcid.org/0000-0001-6139-6887

Junhao Chu − *Technical Center for Multifunctional Magneto-Optical Spectroscopy (Shanghai), Engineering Research Center of Nanophotonics & Advanced Instrument (Ministry of Education), Department of Materials, School of Physics and Electronic Science, East China Normal University, Shanghai 200241, P. R. China; Collaborative Innovation Center of Extreme Optics, Shanxi University, Taiyuan, Shanxi 030006, P. R. China; Shanghai Institute of Intelligent Electronics & Systems, Fudan University, Shanghai 200433, P. R. China*

Complete contact information is available at: https://pubs.acs.org/10.1021/acsami.1c22983

Author Contributions

The manuscript was written through contributions of all authors. All authors have given approval to the final version of the manuscript.

Notes

The authors declare no competing financial interest.

■ ACKNOWLEDGMENTS

This work was financially supported by the National Key Research and Development Program of China (Grants No. 2019YFB2203400), the National Natural Science Foundation of China (Grant Nos. 61974043, 62090013, 12104156, 61974044, and 91833303), the Projects of Science and Technology Commission of Shanghai Municipality (Grant Nos. 21JC1402100 and 19511120100), China Postdoctoral Science Foundation (2020TQ0099, and 2020M681222), the Program for Professor of Special Appointment (Eastern Scholar) at Shanghai Institutions of Higher Learning. A.C. acknowledges the assistance of F. Liu and L. Zheng (Shandong University) with the dielectric response characterizations.

■ REFERENCES

(1) Qiu, C.; Wang, B.; Zhang, N.; Zhang, S.; Liu, J.; Walker, D.; Wang, Y.; Tian, H.; Shrout, T. R.; Xu, Z.; Chen, L.-Q.; Li, F.

Transparent Ferroelectric Crystals with Ultrahigh Piezoelectricity. *Nature* **2020**, *577*, 350−354.
(2) Zhang, S. J.; Li, F. High Performance Ferroelectric Relaxor-$PbTiO_3$ Single Crystals: Status and Perspective. *J. Appl. Phys.* **2012**, *111*, 031301.
(3) Tian, J.; Han, P.; Huang, X.; Pan, H.; Carroll, J. F.; Payne, D. A. Improved Stability for Piezoelectric Crystals Grown in the Lead Indium Niobate-lead Magnesium Niobate Lead Titanate System. *Appl. Phys. Lett.* **2007**, *91*, 222903.
(4) Kumar, A.; Baker, J. N.; Bowes, P. C.; Cabral, M. J.; Zhang, S.; Dickey, E. C.; Irving, D. L.; LeBeau, J. M. Atomic-Resolution Electron Microscopy of Nanoscale Local Structure in Lead-Based Relaxor Ferroelectrics. *Nat. Mater.* **2021**, *20*, 62−67.
(5) Kutnjak, Z.; Petzelt, J.; Blinc, R. The Giant Electromechanical Response in Ferroelectric Relaxors as A Critical Phenomenon. *Nature* **2006**, *441*, 956.
(6) Wang, Y.; Wang, Z.; Ge, W.; Luo, C.; Li, J.; Viehland, D.; Chen, J.; Luo, H. Temperature-Induced and Electric-Field-Induced Phase Transitions in Rhombohedral $Pb(In_{1/2}Nb_{1/2})O_3$-$Pb(Mg_{1/3}Nb_{2/3})O_3$-$PbTiO_3$ Ternary Single Crystals. *Phys. Rev. B* **2014**, *90*, 134107.
(7) Zhang, S.; Luo, J.; Hackenberger, W.; Shrout, T. R. Characterization of $Pb(In_{1/2}Nb_{1/2})O_3$-$Pb(Mg_{1/3}Nb_{2/3})O_3$-$PbTiO_3$ Ferroelectric Crystal with Enhanced Phase Transition Temperatures. *J. Appl. Phys.* **2008**, *104*, 064106.
(8) Huo, X.; Zhang, S.; Liu, G.; Zhang, R.; Luo, J.; Sahul, R.; Cao, W.; Shrout, T. R. Complete Set of Elastic, Dielectric, and Piezoelectric Constants of $[011]_c$ Poled Rhombohedral $Pb(In_{0.5}Nb_{0.5})O_3$-$Pb(Mg_{1/3}Nb_{2/3})O_3$-$PbTiO_3$: Mn Single Crystals. *J. Appl. Phys.* **2013**, *113*, 074106.
(9) Kalinin, S. V.; Rodriguez, B. J.; Budai, J. D.; Jesse, S.; Morozovska, A. N.; Bokov, A. A.; Ye, Z.-G. Direct Evidence of Mesoscopic Dynamic Heterogeneities at the Surfaces of Ergodic Ferroelectric Relaxors. *Phys. Rev. B* **2010**, *81*, 064107.
(10) Bokov, A. A.; Ye, Z.-G. Recent Progress in Relaxor Ferroelectrics with Perovskite Structure. *J. Mater. Sci.* **2006**, *41*, 31−52.
(11) Maier, B.; Mihailova, B.; Paulmann, C.; Ihringer, J.; Gospodinov, M.; Stosch, R.; Guettler, B.; Bismayer, U. Effect of Local Elastic Strain on the Structure of Pb-Based Relaxors: A Comparative Study of Pure and Ba- and Bi-Doped $PbSc_{0.5}Nb_{0.5}O_3$. *Phys. Rev. B* **2009**, *79*, 224108.
(12) Shvartsman, V. V.; Dkhil, B.; Kholkin, A. L. Mesoscale Domains and Nature of the Relaxor State by Piezoresponse Force Microscopy. *Annu. Rev. Mater. Res.* **2013**, *43*, 423−449.
(13) Li, F.; Zhang, S. J.; Yang, T. N.; Xu, Z.; Zhang, N.; Liu, G.; Wang, J. J.; Wang, J. L.; Cheng, Z. X.; Ye, Z. G.; Luo, J.; Shrout, T. R.; Chen, L. Q. The Origin of Ultrahigh Piezoelectricity in Relaxor-Ferroelectric Solid Solution Crystals. *Nat. Commun.* **2016**, *7*, 13807.
(14) Fu, H.; Cohen, R. Polarization Rotation Mechanism for Ultrahigh Electromechanical Response in Single-Crystal Piezoelectrics. *Nature* **2000**, *403*, 281.
(15) Kholkin, A.; Morozovska, A.; Kiselev, D.; Bdikin, I.; Rodriguez, B.; Wu, P.; Bokov, A.; Ye, Z.-G.; Dkhil, B.; Chen, L.-Q.; Kosec, M.; Kalinin, S. V. Surface Domain Structures and Mesoscopic Phase Transition in Relaxor Ferroelectrics. *Adv. Funct. Mater.* **2011**, *21*, 1977−1987.
(16) Li, S.; Eastman, J. A.; Newnham, R. E.; Cross, L. E. Diffuse Phase Transition in Ferroelectrics with Mesoscopic Heterogeneity: Mean-field Theory. *Phys. Rev. B* **1997**, *55*, 12067.
(17) Xu, G.; Wen, J.; Stock, C.; Gehring, P. M. Phase Instability induced by Polar Nanoregions in A Relaxor Ferroelectric System. *Nat. Mater.* **2008**, *7*, 562.
(18) He, W.; Li, Q.; Sun, Y.; Xi, X.; Zhang, Y.; Yan, Q. Investigation of Piezoelectric Property and Nanodomain Structures for PIN-PZ-PMN-PT Single Crystals as A Function of Crystallographic Orientation and Temperature. *J. Mater. Chem. C* **2017**, *5*, 2459−2465.
(19) Paull, O.; Xu, C.; Cheng, X.; Zhang, Y.; Xu, B.; Kelley, K. P.; de Marco, A.; Vasudevan, R. K.; Bellaiche, L.; Nagarajan, V.; Sando, D. Anisotropic Epitaxial Stabilization of A Low-Symmetry Ferroelectric with Enhanced Electromechanical Response. *Nat. Mater.* **2022**, *21*, 74−80.
(20) Xu, G. Competing Orders in PZN-*x*PT and PMN-*x*PT Relaxor Ferroelectrics. *J. Phys. Soc. Jpn.* **2010**, *79*, 011011.
(21) Manley, M.E.; Lynn, J.W.; Abernathy, D.L.; Specht, E.D.; Delaire, O.; Bishop, A.R.; Sahul, R.; Budai, J.D. Phonon Localization Drives Polar Nanoregions in A Relaxor Ferroelectric. *Nature Commun.* **2014**, *5*, 3683.
(22) Zhang, Y.; Xue, D.; Wu, H.; Ding, X.; Lookman, T.; Ren, X. Adaptive Ferroelectric State at Morphotropic Phase Boundary: Coexisting Tetragonal and Rhombohedral Phases. *Acta Mater.* **2014**, *71*, 176−184.
(23) Wang, R.; Yang, B.; Luo, Z.; Sun, E.; Sun, Y.; Xu, H.; Zhao, J.; Zheng, L.; Zhou, H.; Gao, C.; Cao, W. Local twin Domains and Tip-Voltage-Induced Domain Switching of Monoclinic Mc phase in $Pb(Mg_{1/3}Nb_{2/3})O_3$-0.34$PbTiO_3$ Single Crystal Revealed by Piezoresponse Force Microscopy. *Phys. Rev. B* **2016**, *94*, 054115.
(24) Vanderbilt, D.; Cohen, M. H. Monoclinic and Triclinic Phases in Higher-order Devonshire Theory. *Phys. Rev. B* **2001**, *63*, 094108.
(25) Cao, H.; Li, J.; Viehland, D.; Xu, G. Fragile Phase Stability in (1-x)$Pb(Mg_{1/3}Nb_{2/3}O_3)$-x$PbTiO_3$ Crystals: A Comparison of [001] and [110] Field-Cooled Phase Diagrams. *Phys. Rev. B* **2006**, *73*, 184110.
(26) Cao, H.; Bai, F.; Wang, N.; Li, J.; Viehland, D.; Xu, G.; Shirane, G. Intermediate Ferroelectric Orthorhombic and Monoclinic M_B Phases in [110] Electric-Field-Cooled $Pb(Mg_{1/3}Nb_{2/3})O_3$-30% $PbTiO_3$ Crystals. *Phys. Rev. B* **2005**, *72*, 064104.
(27) Rafalovskyi, I.; Guennou, M.; Gregora, I.; Hlinka, J. Macroscopic Lamellar Heterophase Pattern in $Pb(Mg_{1/3}Nb_{2/3})O_3$-$PbTiO_3$ Single Crystals. *Phys. Rev. B* **2016**, *93*, 064110.
(28) Yang, Y.; Liu, Y. L.; Zhang, L. Y.; Zhu, K.; Ma, S. Y.; Siu, G. G.; Xu, Z. K.; Luo, H. S. Polarized Raman Mapping Study of the Microheterogeneity in 0.67$PbMg_{1/3}Nb_{2/3}O_3$-0.33$PbTiO_3$ Single Crystal. *J. Raman Spectrosc.* **2010**, *41*, 1735.
(29) Hu, Q.; Alikin, D. O.; Zelenovskiy, P. S.; Ushakov, A. D.; Chezganov, D. S.; Bian, J.; Zhao, Y.; Tian, Y.; Zhuang, Y.; Li, J.; Jin, L.; Xu, Z.; Shur, V. Y.; Wei, X. Phase Distribution and Corresponding Piezoelectric Responses in A Morphotropic Phase Boundary Pb-$(Mg_{1/3}Nb_{2/3})O_3$-$PbTiO_3$ Single Crystal Revealed by Confocal Raman Spectroscopy and Piezo-Response Force Microscopy. *J. Eur. Ceram. Soc.* **2019**, *39*, 4131−4138.
(30) Wu, F.; Yang, B.; Sun, E.; Zhang, R.; Xu, D.; Zhou, J.; Cao, W. Polarized Raman Study on Phase Transitions in 0.24$Pb(In_{1/2}Nb_{1/2})$-O_3-0.43$Pb(Mg_{1/3}Nb_{2/3})O_3$-0.33$PbTiO_3$ Single Crystal. *J. Alloys Compd.* **2013**, *55*, 198−100.
(31) Bao, P.; Yan, F.; Lu, X.; Zhu, J.; Shen, H.; Wang, Y.; Luo, H. Coexistence of M_A and M_C Phases in $Pb(Mg_{1/3}Nb_{2/3})_{0.68}Ti_{0.32}O_3$ Single Crystals. *Appl. Phys. Lett.* **2006**, *88*, 092905.
(32) Wang, D.; Cao, M.; Zhang, S. J. Phase Diagram and Properties of $Pb(In_{1/2}Nb_{1/2})O_3$-$Pb(Mg_{1/3}Nb_{2/3})O_3$-$PbTiO_3$ Polycrystalline Ceramics. *J. Eur. Ceram. Soc.* **2012**, *32*, 433−439.
(33) Luo, N.; Li, Q.; Xia, Z.; Chu, X. Phase Diagram, Temperature Stability, and Electrical Properties of (0.85-*x*)$Pb(Mg_{1/3}Nb_{2/3})O_3$-0.10$Pb(Fe_{1/2}Nb_{1/2})O_3$-0.05$PbZrO_3$-x$PbTiO_3$ System. *J. Am. Ceram. Soc.* **2012**, *95*, 3246−3253.
(34) Viehland, D.; Jang, S. J.; Cross, L. E.; Wuttig, M. Freezing of the Polarization Fluctuations in Lead Magnesium Niobate Relaxors. *J. Appl. Phys.* **1990**, *68*, 2916.
(35) Tagantsev, A. K. Vogel-Fulcher Relationship for the Dielectric Permittivity of Relaxor Ferroelectrics. *Phys. Rev. Lett.* **1994**, *72*, 1100.
(36) Liu, G.; Kong, L. P.; Hu, Q.; Zhang, S. J. Diffused Morphotropic Phase Boundary in Relaxor-$PbTiO_3$ Crystals: High Piezoelectricity with Improved Thermal Stability. *Appl. Phys. Rev.* **2020**, *7*, 021405.
(37) Li, K.; Sun, E.; Qi, X.; Yang, B.; Liu, J.; Cao, W. Dielectric Relaxation and Local Domain Structures of Ferroelectric PIMNT and PMNT Single Crystals. *J. Am. Ceram. Soc.* **2020**, *103*, 1744−1754.
(38) Zhu, J. J.; Jiang, K.; Xu, G. S.; Hu, Z. G.; Li, Y. W.; Zhu, Z. Q.; Chu, J. H. Temperature-Dependent Raman Scattering and Multiple

https://doi.org/10.1021/acsami.1c22983
ACS Appl. Mater. Interfaces 2022, 14, 10535−10545

Phase Coexistence in Relaxor Ferroelectric $Pb(In_{1/2}Nb_{1/2})O_3$-$Pb(Mg_{1/3}Nb_{2/3})O_3$-$PbTiO_3$ Single Crystals. *J. Appl. Phys.* **2013**, *114*, 153508.
(39) Lima, J. A.; Paraguassu, W.; Freire, P. T. C.; Souza Filho, A. G.; Paschoal, C. W. A.; Filho, J. M.; Zanin, A. L.; Lente, M. H.; Garcia, D.; Eiras, J. A. Lattice Dynamics and Low-Temperature Raman Spectroscopy Studies of PMN-PT Relaxors. *J. Raman Spectrosc.* **2009**, *40*, 1144.
(40) Prosandeev, S. A.; Cockayne, E.; Burton, B. P.; Kamba, S.; Petzelt, J.; Yuzyuk, Y.; Katiyar, R. S.; Vakhrushev, S. B. Lattice Dynamics in $PbMg_{1/3}Nb_{2/3}O_3$. *Phys. Rev. B* **2004**, *70*, 134110.
(41) Ye, Y.; Cui, A. Y.; Bian, M.; Jiang, K.; Zhu, L. Q.; Zhang, J. Z.; Shang, L. Y.; Li, Y. W.; Hu, Z. G.; Chu, J. H. Temperature and Pressure Manipulation of Magnetic Ordering and Phonon Dynamics with Phase Transition in Multiferroic $GdFeO_3$: Evidence from Raman Scattering. *Phys. Rev. B* **2020**, *102*, 024103.
(42) Cui, A. Y.; Cao, X. H.; Ye, Y.; Jiang, K.; Zhu, L. Q.; Jiang, M. H.; Rao, G. H.; Li, Y. W.; Hu, Z. G.; Chu, J. H. Phase Transitions and Phonon Thermodynamics in Giant Piezoelectric Mn-doped $K_{0.5}Na_{0.5}NbO_3$-$LiBiO_3$ Crystals Studied by Raman Spectroscopy. *Phys. Rev. B* **2020**, *102*, 214102.
(43) Cui, A. Y.; Ye, Y.; Zheng, L.; Jiang, K.; Zhu, L. Q.; Shang, L. Y.; Li, Y. W.; Hu, Z. G.; Chu, J. H. Exploring Lattice Symmetry Evolution with Discontinuous Phase Transition by Raman Scattering Criteria: The Single-crystalline $(K,Na)NbO_3$ Model System. *Phys. Rev. B* **2019**, *100*, 024102.
(44) Pan, H.; Li, F.; Liu, Y.; Zhang, Q.; Wang, M.; Lan, S.; Zheng, Y.; Ma, J.; Gu, L.; Shen, Y.; Yu, P.; Zhang, S.; Chen, L.-Q.; Lin, Y.-H.; Nan, C.-W. Ultrahigh-Energy Density Lead-free Dielectric Films via Polymorphic Nanodomain Design. *Science* **2019**, *365*, 578−582.
(45) Tao, H.; Wu, H.; Liu, Y.; Zhang, Y.; Wu, J.; Li, F.; Lyu, X.; Zhao, C.; Xiao, D.; Zhu, J.; Pennycook, S. J. Ultrahigh Performance in Lead-Free Piezoceramics Utilizing A Relaxor Slush Polar State with Multiphase Coexistence. *J. Am. Chem. Soc.* **2019**, *141*, 13987−13994.
(46) Jin, Y. M.; Wang, Y. U.; Khachaturyan, A. G.; Li, J. F.; Viehland, D. Conformal Miniaturization of Domains with Low Domain-Wall Energy: Monoclinic Ferroelectric States near the Mmorphotropic Phase Boundaries. *Phys. Rev. Lett.* **2003**, *91*, 197601.
(47) Bellaiche, L.; García, A.; Vanderbilt, D. Finite-Temperature Properties of $Pb(Zr_{1-x}Ti_x)O_3$ Alloys from First Principles. *Phys. Rev. Lett.* **2000**, *84*, 5427.
(48) Bowles, J. S.; Mackenzie, J. K. The Crystallography of Martensite Transformations I. *Acta Metall* **1954**, *2*, 129.
(49) Khachaturyan, A. G. *The Theory of Structural Transformations in Solids*; Wiley: New York, 1983; p 213.
(50) Ge, W.; Zhu, W.; Tang, T.; Pezzotti, G. Quantitative Evaluation of Local Domain Patterns in [110] Poled $Pb(Mg_{1/3}Nb_{2/3})O_3$-$0.35PbTiO_3$ Single Crystal Using A Polarized Raman Microprobe. *Appl. Phys. Lett.* **2009**, *94*, 112905.
(51) Zallen, R.; Conwell, E. M. The Effect of Temperature on Libron Frequencies in Molecular Crystals: Implications for TTF-TCNQ. *Solid State Commun.* **1979**, *31*, 557.
(52) Zallen, R.; Slade, M. L. Influence of Pressure and Temperature on Phonons in Molecular Chalcogenides: Crystalline As_4S_4 and S_4N_4. *Phys. Rev. B* **1978**, *18*, 5775.
(53) Ouyang, J.; Roytburd, A. L. Theoretical Modeling of Coexisting Tetragonal and Rhombohedral Heterophase Polydomain Structures in Lead Zirconate Titanate Ferroelectric Films near the Morphotropic Phase Boundary. *Acta Mater.* **2006**, *54*, 5565.
(54) Ouyang, J.; Zhang, W.; Huang, X.; Roytburd, A. L. Thermodynamics of Formation of Tetragonal and Rhombohedral Heterophase Polydomains in Epitaxial Ferroelectric Thin Films. *Acta Mater.* **2011**, *59*, 3779.
(55) Liu, H.; Chen, J.; Fan, L.; Ren, Y.; Pan, Z.; Lalitha, K. V.; Rödel, J.; Xing, X. Critical Role of Monoclinic Polarization Rotation in High-Performance Perovskite Piezoelectric Materials. *Phys. Rev. Lett.* **2017**, *119*, 017601.
(56) Liu, W.; Ren, X. Large Piezoelectric Effect in Pb-Free Ceramics. *Phys. Rev. Lett.* **2009**, *103*, 257602.
(57) Xu, G.; Chen, K.; Yang, D.; Li, J. Growth and Electrical Properties of Large Size $Pb(In_{1/2}Nb_{1/2})O_3$-$Pb(Mg_{1/3}Nb_{2/3})O_3$-$PbTiO_3$ Crystals Prepared by the Vertical Bridgman Technique. *Appl. Phys. Lett.* **2007**, *90*, 032901.
(58) Cui, A. Y.; Wolf, P. D.; Ye, Y.; Hu, Z. G.; Dujardin, A.; Huang, Z. Q.; Jiang, K.; Shang, L. Y.; Ye, M.; Sun, H.; Chu, J. H. Probing Electromechanical Behaviors by Datacube Piezoresponse Force Microscopy in Ambient and Aqueous Environments. *Nanotechnology* **2019**, *30*, 235701.
(59) Porto, S. *Porto's Notation, Bilbao Crystallographic, Raman Scattering*, http://www.cryst.ehu.es/cgi-bin/cryst/programs/nph-doc-raman.

https://doi.org/10.1021/acsami.1c22983
ACS Appl. Mater. Interfaces 2022, 14, 10535−10545